Interleaved Bidirectional Chopper With Auxiliary Converters for DC Electric Railways

Hamzeh J. Ahmad, *Student Member, IEEE*, and Makoto Hagiwara, *Senior Member, IEEE*

***Abstract*—This article presents an interleaved bidirectional chopper with auxiliary converters for onboard energy storage systems that is capable of achieving a significant reduction in the mass and volume of the current-smoothing inductors. The proposed chopper consists of multiple interleaved subconverters, where each subconverter consists of a bidirectional chopper cell, a current-smoothing inductor at the low-voltage side, and an auxiliary converter that is formed by the cascade connection of multiple full-bridge cells. Each auxiliary converter is connected in series with its respective inductor to suppress the ac voltage component that produces ripple current in the inductor of each subconverter; hence, a smaller inductor can be used to meet the ripple current requirement when compared with the conventional bidirectional chopper. In addition, auxiliary converters can be used as dc-circuit breakers to protect the low-voltage side against faults in the power devices of the bidirectional chopper cells. This article discusses the operating principles and control method of the proposed chopper, followed by experiments using a downscaled experimental model.**

***Index Terms*—Battery energy storage system, dc circuit breaker, dc–dc converter.**

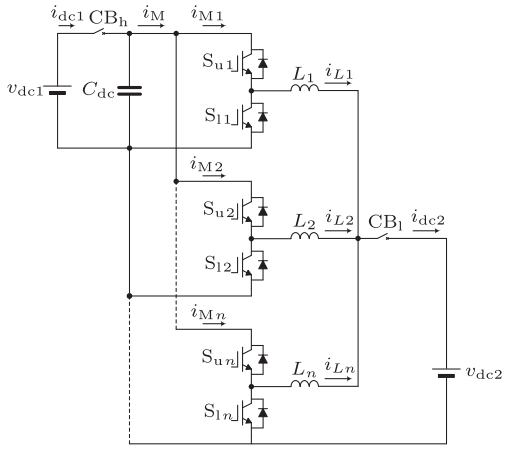

Fig. 1. Circuit configuration of a conventional interleaved bidirectional chopper for dc electric railways.

I. Introduction

ENERGY storage systems that are based on lithium ion batteries, nickel-metal hydride batteries, electric double layer capacitors, fuel cells, and flywheels are used in dc electric railways as power sources [1]–[10]. In particular, battery energy storage systems (BESS) that are placed inside the dc electric railways (i.e., onboard storage systems) allow the regenerative energy to be stored during breaking and reused when it is required [11]–[13]. Further, the catenary voltage drop during acceleration can be limited, because the onboard BESS can be used to supply the peak power [11]. Meanwhile, the onboard BESS can supply power when there is a break in the overhead lines or when the train is running on a nonelectrified section. Catenary-free operation may be required when there is a limitation on the level of visual intrusion, or when the infrastructure of the overhead electrification is not economically feasible [14]. However, the onboard BESS adds to the mass and volume of the moving railway vehicle [15].

Manuscript received June 28, 2020; revised August 31, 2020; accepted October 3, 2020. Date of publication October 16, 2020; date of current version January 22, 2021. Recommended for publication by Associate Editor X. Wu. *(Corresponding author: Hamzeh J. Ahmad.)*

The authors are with the Department of Electrical and Electronic Engineering, Tokyo Institute of Technology, Tokyo 152-8552, Japan (e-mail: ahmad.h.ab@m.titech.ac.jp; hagiwara@ee.e.titech.ac.jp).

Color versions of one or more of the figures in this article are available online at https://ieeexplore.ieee.org.

Digital Object Identifier 10.1109/TPEL.2020.3031668

Typically, dc electrification systems with voltages ranging from 600 V to 3 kV are adopted in dc electric railways [16], [17]. A bidirectional chopper is required for voltage conversion between the voltage level of the catenary and that of the battery, and for allowing the regenerative braking energy to be stored in the battery. It is noteworthy that the capacity of a bidirectional chopper can be as high as 500 kW [3]. Fig. 1 shows the circuit configuration of a conventional interleaved bidirectional chopper which is formed by interleaving multiple subconverters, where each subconverter consists of a bidirectional chopper cell and a current-smoothing inductor. v_{dc1} is the dc voltage at the high-voltage side which corresponds to a dc catenary voltage, and v_{dc2} is the dc voltage at the low-voltage side which corresponds to the BESS voltage. CB_h and CB_l are the high-voltage side and the low-voltage side dc-circuit breakers which are installed for protecting the system from short-circuit faults in the power devices [3], [10], [18]–[20].

High-power choppers suffer from bulky and heavy magnetics, since the operating switching frequencies are limited because of the limitation of the power losses in the power devices. For example, the switching frequency of 3.3-kV Si-IGBTs is typically set to less than one kilohertz for reducing switching loss. It is required to reduce the mass and volume of the onboard bidirectional chopper since the mass affects the driving range while the volume affects the flexibility of the vehicle design [21]. The mass and volume of the chopper strongly depend on those of the high-power inductor which can be the single bulkiest and heaviest component in the converter system [22].

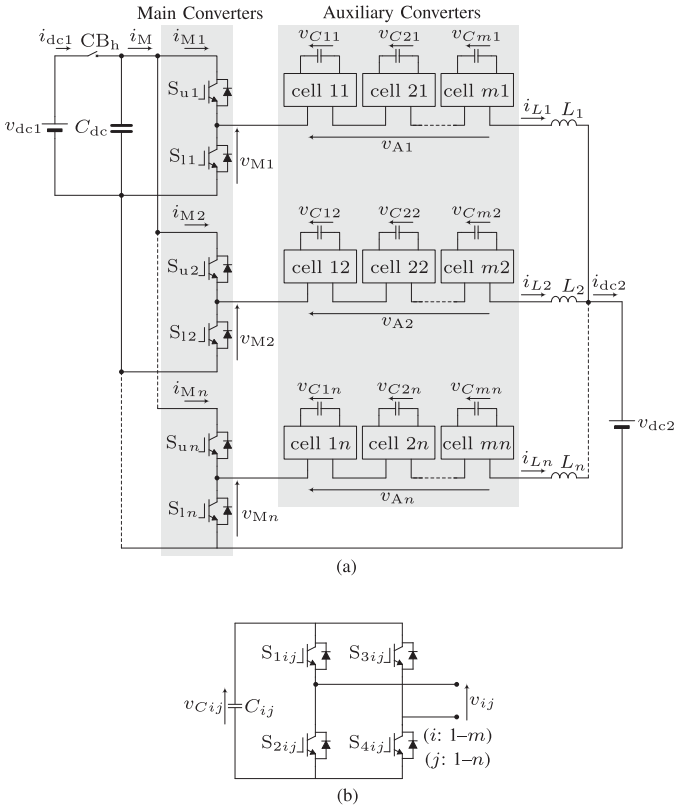

Fig. 2. Interleaved bidirectional chopper with auxiliary converters. (a) Overall configuration. (b) Bridge cell.

This article proposes an interleaved bidirectional chopper with auxiliary converters that is intended for its application to onboard BESS in dc electric railways. The proposed chopper is capable of achieving the same peak-to-peak ripple current as that produced by the conventional interleaved chopper using smaller current-smoothing inductors. A smoother high-voltage-side current can be obtained as a result of interleaving, which further reduces the mass and volume of the magnetics required for current smoothing. Moreover, the proposed chopper can interrupt fault currents at the low-voltage side. Hence, mechanical circuit breakers at the low-voltage side can be removed. There is no paper in the past works with a focus on the interleaved bidirectional chopper with auxiliary converters with experimental verification.

The rest of this article is organized as follows: Section II presents the proposed circuit configuration. Section III and IV discuss the principles of operation and control method of the proposed chopper. Section V presents the experimental verification using a down-scaled experimental model. In Section VI, the proposed chopper and the conventional chopper are compared in terms of volume, mass, and efficiency. Finally, the article is concluded in Section VII.

II. Circuit Configuration

Fig. 2(a) shows the circuit configuration of an interleaved bidirectional chopper with auxiliary converters (IBCAC). A parallel connection of n subconverters forms the IBCAC, where each subconverter consists of a bidirectional chopper cell, a cascade connection of m full-bridge cells, and a current-smoothing inductor, L_j (j: 1–n). In each subconverter, the bidirectional chopper cell is called a main converter, while a cascade connection of m full-bridge cells is called an auxiliary converter. Fig. 2(a) is equivalent to a conventional interleaved bidirectional chopper if the auxiliary converters are eliminated.

In Fig. 2(a), $v_{\rm dc1}$ and $C_{\rm dc}$ are the voltage source and dc-link capacitor at the high-voltage side. $\rm S_{uj}$ and $\rm S_{lj}$ are the upper and lower power devices of each main converter. At the high-voltage side, $i_{\rm dc1}$ is the dc current sourced from $v_{\rm dc1}$, $i_{\rm M}$ is the total current flowing to the main converters, $i_{{\rm M}j}$ is the current flowing to each main converter, and $v_{{\rm M}j}$ is the voltage produced by each main converter. Meanwhile, $v_{\rm dc2}$ is the voltage source at the low-voltage side, i_{Lj} is the inductor current of each subconverter, and $i_{\rm dc2}$ is the current flowing to $v_{\rm dc2}$. $v_{{\rm A}j}$ is the sum of the individual cell voltages produced by each full-bridge cell. Fig. 2(b) shows the circuit configuration of the full-bridge cell forming the auxiliary converter, where v_{Cij} (i: 1–m) denotes the dc-capacitor voltage, v_{ij} is the ac output voltage, $\rm S_{1ij}$, $\rm S_{2ij}$, $\rm S_{3ij}$, and $\rm S_{4ij}$ are the power devices.

A dc circuit breaker, $\rm CB_h$, should be installed in series with $v_{\rm dc1}$ as shown in Fig. 2(a) to protect the system from short-circuit faults in the power devices of the main converters. In the conventional interleaved bidirectional chopper, another dc circuit breaker should be installed in series with $v_{\rm dc2}$ for protecting the system from the short-circuit fault. However, this additional dc circuit breaker is unnecessary to be installed in Fig. 2(a) because the auxiliary converters can work as solid-state dc circuit breakers, which will be verified experimentally later on.

III. Principles of Operation

The main advantages of the IBCAC can be summarized as follows.

1) A much smaller L_j can be used compared with the conventional interleaved bidirectional chopper to achieve the same peak-to-peak ripple current in $i_{\rm dc2}$.
2) The auxiliary converters can work as solid-state dc circuit breakers during the fault.
3) $i_{\rm M}$ can be a much smoother wave by interleaving multiple subconverters, although this feature is also achievable by the conventional interleaved chopper.

A. Principles of Operation of the Main Converters

The dead-time period, where $\rm S_{uj}$ and $\rm S_{lj}$ are simultaneously OFF is assumed to be zero in the following analysis. Similar to Fig. 1, the voltage produced by each main converter, $v_{{\rm M}j}$, is given by

$$v_{{\rm M}j} = \begin{cases} v_{\rm dc1} & (\rm S_{uj}: ON,\ S_{lj}: OFF) \\ 0 & (\rm S_{uj}: OFF,\ S_{lj}: ON). \end{cases} \tag{1}$$

$v_{{\rm M}j}$ can be divided into a dc component, $(v_{{\rm M}j})_{\rm dc}$, and an ac component, $(v_{{\rm M}j})_{\rm ac}$, where the former is given by

$$(v_{{\rm M}j})_{\rm dc} = d_{{\rm M}j} v_{\rm dc1} \tag{2}$$

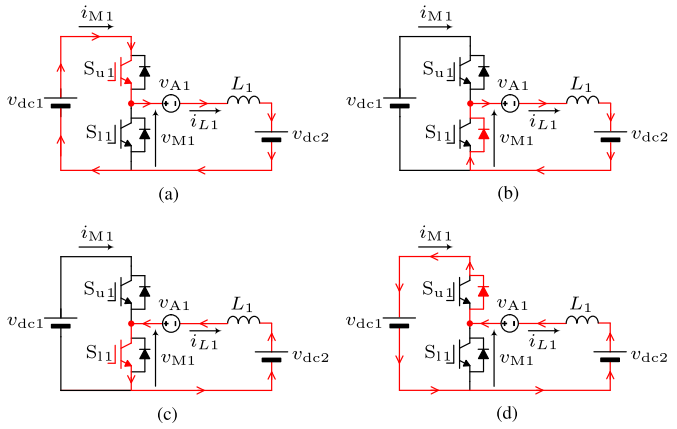

Fig. 3. Circuit configuration of a subconverter of the IBCAC. (a) S_{u1} is ON, and i_{L1} is positive. (b) S_{l1} is ON, and i_{L1} is positive. (c) S_{l1} is ON, and i_{L1} is negative. (d) S_{u1} is ON, and i_{L1} is negative.

where d_{Mj} is the instantaneous duty ratio of S_{uj}. $(v_{Mj})_{ac}$ is a square wave with a frequency of f_{SM}, which is the switching frequency of the main converters, and it is given by

$$(v_{Mj})_{ac} = \begin{cases} (1-d_{Mj})v_{dc1} & (S_{uj}: \text{ON},\ S_{lj}: \text{OFF}) \\ -d_{Mj}v_{dc1} & (S_{uj}: \text{OFF},\ S_{lj}: \text{ON}). \end{cases} \quad (3)$$

B. Principles of Operation of the Auxiliary Converters

The primary function of the auxiliary converter in each subconverter is to produce an ac voltage $(v_{Aj})_{ac}$ that is equal to $(v_{Mj})_{ac}$ to cancel out the ac voltage component that produces the ripple current. $(v_{Aj})_{ac}$ is given by

$$(v_{Aj})_{ac} = \begin{cases} (1-d_{Mj})v_{dc1} & (S_{uj}: \text{ON},\ S_{lj}: \text{OFF}) \\ -d_{Mj}v_{dc1} & (S_{uj}: \text{OFF},\ S_{lj}: \text{ON}). \end{cases} \quad (4)$$

Consequently, no ac component is superimposed on the inductor, L_j, and each inductor current, i_{Lj}, produces no switching-ripple currents ideally. In an actual system, a switching-ripple current stemming from the phase-shifted pulse width modulation (PWM) applied to each auxiliary converter occurs in i_{Lj}. However, this switching-ripple current is much smaller and easier to mitigate owing to the high equivalent switching frequency of the auxiliary converter [23]–[25]. Specifically, the equivalent switching frequency when the phase-shifted PWM is applied is $2mf_{SA}$, where m is the bridge-cell count and f_{SA} is the switching frequency of each cell. In addition, the amplitude of the switching-ripple voltage can be smaller than that of the conventional chopper owing to a good effect of the phase-shifted PWM.

Fig. 3 shows the current-flow path and the conducting power devices of a subconverter of the IBCAC during each state of normal operation, where the current-flow path and the conducting power devices are marked in red. Fig. 3(a) shows the circuit configuration of a subconverter of the IBCAC when S_{u1} is ON, S_{l1} is OFF, and i_{L1} is positive. In this case, v_{M1} equals v_{dc1}, and v_{A1} is controlled to equal $(1-d_{M1})v_{dc1}$. Fig. 3(b) shows the circuit configuration when S_{u1} is OFF, S_{l1} is ON, and i_{L1} is positive. In this case, v_{M1} equals zero, and v_{A1} is controlled to equal $-d_{M1}v_{dc1}$. Hence, the voltage difference between the v_{M1} and v_{A1} (i.e., $v_{M1}-v_{A1}$) equals $(v_{Mj})_{dc}$, which ideally equals v_{dc2}. As a result, the voltage across the inductor becomes zero and a pure dc current flows through it, where i_{M1} equals zero when S_{u1} is OFF and equals i_{L1} when S_{u1} is ON. The ideal voltage and current waveforms of a subconverter of the IBCAC are shown in Fig. 4. Another attractive function of the auxiliary converters is that they can work as solid-state dc circuit breakers disconnecting v_{dc2} from the rest of the converter system when a short-circuit fault occurs in the power device(s) of the main converters. This function can be realized by turning OFF all the power devices of the auxiliary converters. Consequently, the low-voltage-side dc circuit breaker that should be installed in the conventional bidirectional chopper can be removed. As a result, the mass, volume, and cost of the system can be reduced. However, the high-voltage-side dc circuit breaker, CB_h, is indispensable.

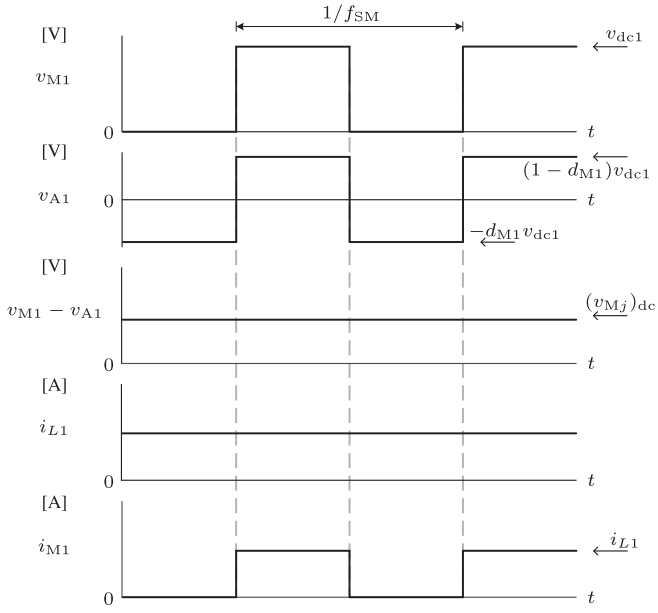

Fig. 4. Ideal voltage and current waveforms of a subconverter of the IBCAC.

It is noteworthy that the dc capacitors of each cell should be initially charged and kept to an initial voltage of v_{Cij} for the startup operation. A method for charging the capacitors will be described and verified experimentally later on.

C. Design Considerations

Each auxiliary converter produces an ac voltage, $(v_{Aj})_{ac}$, and an amount of switching-ripple voltage that mainly stems from the PWM operation, turn-ON and turn-OFF times of the power devices, and the effect of dead time. The switching-ripple voltage produces a ripple current in i_{Lj} that should be attenuated to maintain this ripple within a specified design limit. As mentioned above, the amount of the switching-ripple voltage can be mitigated by applying the phase-shifted PWM to each bridge cell, where an initial phase of each carrier wave is phase-shifted by $(180^\circ/m)$ each other, which makes the voltage step and the switching-ripple frequency of v_{Aj} become v_{Cj} and $2mf_{SA}$, respectively, where v_{Cj} is the voltage of each full-bridge

capacitor, assuming that all full-bridge cell capacitor voltages are equal (i.e., $v_{Cij} = v_{Cj}$). The switching-ripple voltage in $v_{\mathrm{A}j}$, $(v_{\mathrm{A}j})_{\mathrm{ripple}}$, can be expressed as

$$(v_{\mathrm{A}j})_{\mathrm{ripple}} = \begin{cases} \frac{v_{Cj}}{2} & (0 < t \le \frac{1}{4mf_{\mathrm{SA}}}) \\ -\frac{v_{Cj}}{2} & (\frac{1}{4mf_{\mathrm{SA}}} < t < \frac{1}{2mf_{\mathrm{SA}}}). \end{cases} \tag{5}$$

Here, a period of time when a positive voltage is produced and the one when a negative voltage is produced are assumed equal for the sake of simplifying analysis. The amplitude of the switching-ripple current, $(i_{Lj})_{\mathrm{ripple}}$, is determined from (5) as

$$(i_{Lj})_{\mathrm{ripple}} = \frac{1}{L_j}\int_0^{\frac{1}{4mf_{\mathrm{SA}}}} \frac{v_{Cj}}{2}dt = \frac{v_{Cj}}{8L_j m f_{\mathrm{SA}}}. \tag{6}$$

When the auxiliary converters are not used, the peak-to-peak value of the switching-ripple current, $(i_{Lj})_{\mathrm{ripple}}$, can be given as

$$(i_{Lj})_{\mathrm{ripple}} = \frac{v_{\mathrm{dc1}}}{L_j f_{\mathrm{SM}}} d_{\mathrm{M}j}(1 - d_{\mathrm{M}j}). \tag{7}$$

Equations (6) and (7) give the amplitude ratio $i_{w/}/i_{w/o}$ as

$$\frac{i_{w/}}{i_{w/o}} = \frac{v_{Cj} f_{\mathrm{SM}}}{8mv_{\mathrm{dc1}} f_{\mathrm{SA}} d_{\mathrm{M}j}(1 - d_{\mathrm{M}j})} \tag{8}$$

where $i_{w/}$ is $(i_{Lj})_{\mathrm{ripple}}$ with the auxiliary converter, and $i_{w/o}$ is $(i_{Lj})_{\mathrm{ripple}}$ without the auxiliary converter. The following relation exists between v_{Cj}, m, and $v_{\mathrm{A}j}$ as

$$-mv_{Cj} \le v_{\mathrm{A}j} \le mv_{Cj}. \tag{9}$$

From (4) and (9), v_{Cj} should satisfy the following conditions:

$$\begin{cases} \frac{(1-d_{\mathrm{M}j})v_{\mathrm{dc1}}}{m} \le v_{Cj} \\ \frac{d_{\mathrm{M}j}v_{\mathrm{dc1}}}{m} \le v_{Cj}. \end{cases} \tag{10}$$

Here, $d_{\mathrm{M}j}$ is produced by the control system of the converter, where it mainly depends on the catenary voltage and battery voltage. Besides, m and v_{Cj} can be used as design variables that can be freely selected as long as (10) is satisfied. Equation (10) implies that v_{Cj} can be decreased by increasing m, producing less switching-ripple current under the same frequencies of f_{SM} and f_{SA} as can be inferred from (8). However, the increase in the bridge-cells count may result in an eventual rise in cost.

f_{SM} is determined by the voltage rating of power device used. For example, it is set from 500 to 1 kHz for 3.3-kV IGBTs and set to more than 1 kHz for 1.2-kV IGBTs. Besides, f_{SA} should be higher than f_{SM} for enabling each bridge cell to produce a square wave with a frequency of f_{SM}. The voltage rating of power devices used in the auxiliary converter is determined by the maximum value of v_{Cj}. For example, it is calculated from (10) as 500 V when $v_{\mathrm{dc1}} = 1500$ V and $m = 3$. In this case, 1.2-kV IGBTs or 1.2-kV SiC-MOSFETs can be used as power devices.

IV. Converter Control

The control system of the IBCAC can be divided into two parts: The main converters control and the auxiliary converters control. The control system of the main converters is responsible for controlling power flow between v_{dc1} and v_{dc2}. Meanwhile, the control system of the auxiliary converters is responsible for mitigating the ripple current included in i_{Lj}, regulating v_{Cij}, and protecting the system by working as solid-state dc-circuit breakers in case of short-circuit faults. It is noteworthy that the control of each main/auxiliary converter is identical and independent of each other.

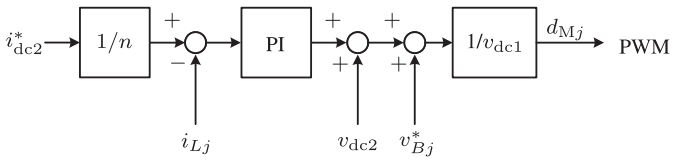

Fig. 5. Control block diagram of the main converters.

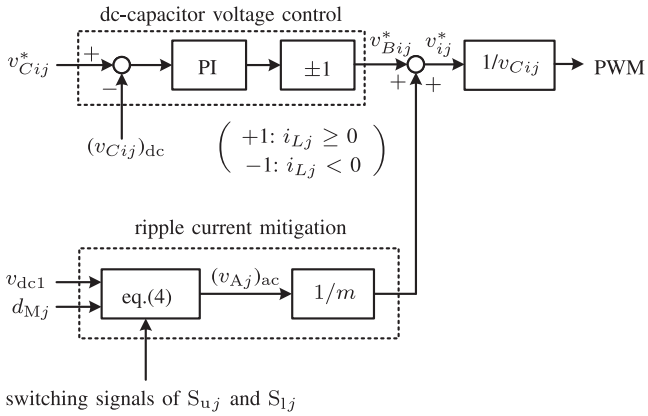

Fig. 6. Control block diagram of the auxiliary converters.

A. Control of the Main Converters

Fig. 5 shows the control block diagram of the main converters, where the current control loop forces the inductor current of each subconverter, i_{Lj}, to follow a reference current, i^*_{dc2}/n, such that each inductor current is independently controlled to carry $1/n$ of i_{dc2}. v_{dc2} and the reference voltage produced by each auxiliary converter for the dc-capacitor voltage control (as described later), v^*_{Bj}, are used as feedforward control to decouple each main converter and the corresponding auxiliary converter in terms of control. The instantaneous duty ratio of each main converter, $d_{\mathrm{M}j}$, is fed to a pulsewidth modulator where the phase-shift between the carriers equals $360^\circ/n$.

B. Control of the Auxiliary Converters

Fig. 6 shows the control block diagram of the auxiliary converters. It consists of the ripple current mitigation and the dc-capacitor voltage control. The function as a solid-state dc circuit breaker is not included in Fig. 6. The ac voltage $(v_{\mathrm{A}j})_{\mathrm{ac}}$ expressed in (4) should be produced by each auxiliary converter to mitigate the ripple current in the inductor current. For this purpose, v_{dc1}, $d_{\mathrm{M}j}$, and the switching signals of each main converter are given as input signals. Each bridge cell in the corresponding auxiliary converter produces an ac voltage $(v_{\mathrm{A}j})_{\mathrm{ac}}/m$.

The dc-capacitor voltage control forces the arithmetic average value of each dc-capacitor voltage $(v_{Cij})_{\mathrm{dc}}$ to follow its reference voltage, v^*_{Cij}, and produces the reference voltage for

TABLE I
SWITCHING MODES FOR THE INITIAL CHARGING OF THE AUXILIARY CONVERTERS

Mode	i_{Lj}	S_{1ij}	S_{2ij}	S_{3ij}	S_{4ij}
Charging mode	$i_{Lj} > 0$	ON	OFF	OFF	ON
	$i_{Lj} < 0$	OFF	ON	ON	OFF
Short-circuit mode 1		ON	OFF	ON	OFF
Short-circuit mode 2		OFF	ON	OFF	ON

the dc-capacitor voltage control, v^*_{Bij}. The sum of v^*_{Bij} of each auxiliary converter, v^*_{Bj}, is given by

$$v^*_{Bj} = \sum_{i=1}^{m} v^*_{Bij} \tag{11}$$

where v_{Bj} $(= v^*_{Bj})$ is a dc quantity that may interfere with the main converters in terms of current control. Therefore, v^*_{Bj} is provided to the main converters control as a feedforward signal to achieve decoupling of control.

In Fig. 6, $(v_{Cij})_{\rm dc}$ is obtained by applying a moving-average filter with a frequency of $f_{\rm SM}$ to v_{Cij}. When the product of v_{Bij} and i_{Lj} (i.e., $v_{Bij}i_{Lj}$) is positive, a positive active power flows into the capacitor and $(v_{Cij})_{\rm dc}$ increases. When the product is negative, a negative active power flows into the capacitor and $(v_{Cij})_{\rm dc}$ decreases. Therefore, the polarity of v^*_{Bij} should be changed depending on the direction of i_{Lj}. Finally, the reference voltages v^*_{ij} are fed to pulsewidth modulators, where the phase-shifted PWM is applied to each auxiliary converter. The phase-shift between carriers of each full-bridge cell equals $180^\circ/m$.

C. Converter Startup

The dc capacitors of each cell should be initially charged using either $v_{\rm dc1}$ or $v_{\rm dc2}$. The relation $i_{Lj} \geq 0$ always holds when $v_{\rm dc1}$ is used, whereas the relation $i_{Lj} \leq 0$ always holds when $v_{\rm dc2}$ is used. The switching states of the power devices in the main and auxiliary converters are adjusted, such that the initial charging of the capacitors is accomplished. Hence, no additional circuits are required for the initial charging.

When $v_{\rm dc1}$ is used for the initial charging, $S_{{\rm u}j}$ is the active switch that controls the charging process and $S_{{\rm l}j}$ is kept OFF. Meanwhile, when $v_{\rm dc2}$ is used for the initial charging, $S_{{\rm l}j}$ is the active switch and $S_{{\rm u}j}$ is kept OFF. The capacitors of each subconverter are charged sequentially in a process that can be called "sequential charging," such that one capacitor is charged at a time. Table I summarizes the switching modes for the initial charging of the auxiliary converters. In each subconverter, a certain cell of the auxiliary converter is operated in the "charging mode" while the remaining cells are operated in the "short-circuit mode." When the charging process of one capacitor is completed, the cell is operated in the short-circuit mode, and the next cell is operated in the charging mode. The process is repeated until all capacitors are charged. When a certain bridge cell is operated in the charging mode and the relation $i_{Lj} \geq 0$ holds, S_{1ij} and S_{4ij} are ON whereas S_{2ij} and S_{3ij} are OFF. In this case, the relation $v_{ij} = v_{Cij}$ holds in Fig. 2(b) and a positive current flows into the capacitor. Consequently, the capacitor voltage increases. The duty ratio of the main converter, $d_{{\rm M}j}$, is different for each capacitor charging process, and it is given by the feedback control of the dc-capacitor voltage in the charging process. For example, when v_{C1j} is being charged, $d_{{\rm M}j}$ is given by

$$d_{{\rm M}j} = K_p(v^*_{C1j} - v_{C1j}) + K_i \int (v^*_{C1j} - v_{C1j})dt \tag{12}$$

where K_p is the proportional gain, and K_i is the integral gain, v^*_{C1j} is its reference. When a certain bridge cell is operated in the charging mode and the relation $i_{Lj} \leq 0$ holds, S_{2ij} and S_{3ij} are ON while S_{1ij} and S_{4ij} are OFF. The short-circuit mode can be realized in two ways; a short-circuit mode 1 and a short-circuit mode 2 as defined in Table I. In the short-circuit mode 1, the power devices of the positive-side arms are ON and those of the negative-side arms are OFF. In the short-circuit mode 2, the power devices of the positive-side arms are OFF and those of the negative-side arms are ON. In both modes, the relation $v_{ij} = 0$ holds and no current flows into the capacitor. Consequently, the capacitor voltage is unchanged during these modes.

D. Circuit Breaker Operation

When a short-circuit occurs in any or both of the power devices of the main converters, the inductor current, i_{Lj}, may increase or decrease, causing an undesirable overcurrent to the system. For protecting the system from the overcurrent, it is necessary to install dc circuit breakers in both high- and low-voltage sides in Fig. 1. Meanwhile, the auxiliary converters have the function of working as solid-state dc circuit breakers that can interrupt the inductor current as mentioned in the previous section. Hence, a dc circuit breaker at the low-voltage side can be removed.

The auxiliary converters can interrupt the inductor current during the fault much faster than mechanical dc circuit breakers, where the fault-current interruption takes typically less than one millisecond. Since no arc occurs in the auxiliary converters, an arc extinguishing mechanism required for the mechanical dc circuit breakers is not required, and the high reliability of the system can be realized.

The IBCAC can detect a short-circuit fault by monitoring i_{Lj}. Specifically, the circuit breaker operation is triggered when it reaches a specified threshold value. The measurement of i_{Lj} is also required for control purposes; therefore, no additional sensors are required for the circuit breaker operation.

V. EXPERIMENTAL RESULTS

A. Experimental Conditions

Table II summarizes the circuit parameters, and Fig. 7 shows a photograph of the down-scaled model used in experiments. In the down-scaled model, the voltage at the high-voltage side was set to $v_{\rm dc1} = 150$ V, and the voltage at the low-voltage side was set to either $v_{\rm dc2} = 50$ V or $v_{\rm dc2} = 75$ V. The reference current was set to either $i^*_{\rm dc2} = +30$ A or $i^*_{\rm dc2} = -30$ A.

Each voltage and current waveform corresponds to those in Fig. 2, whereas only the representative waveforms are shown since the remaining waveforms are similar. For example, $v_{\rm M1}$ is shown, whereas $v_{\rm M2}$ and $v_{\rm M3}$ are not shown since they are

TABLE II
CIRCUIT PARAMETERS USED IN EXPERIMENTS

DC voltage source 1	$v_{\rm dc1}$	150 V
DC voltage source 2	$v_{\rm dc2}$	50 V, 75 V
Inductance at 0 Hz	L_j (0 Hz)	0.75 mH
Inductance at 21.6 kHz	L_j (21.6 kHz)	0.32 mH
Bridge-cell count in each aux. conv.	m	3
Chopper-cell count	n	3
DC-capacitor voltage	v_{Cij}	50 V
Full-bridge cell capacitor	C_{ij}	2.5 mF
High-voltage-side capacitor	$C_{\rm dc}$	4.8 mF
Carrier freq. (chopper cells)	$f_{\rm SM}$	900 Hz
Carrier freq. (full-bridge cells)	$f_{\rm SA}$	3.6 kHz

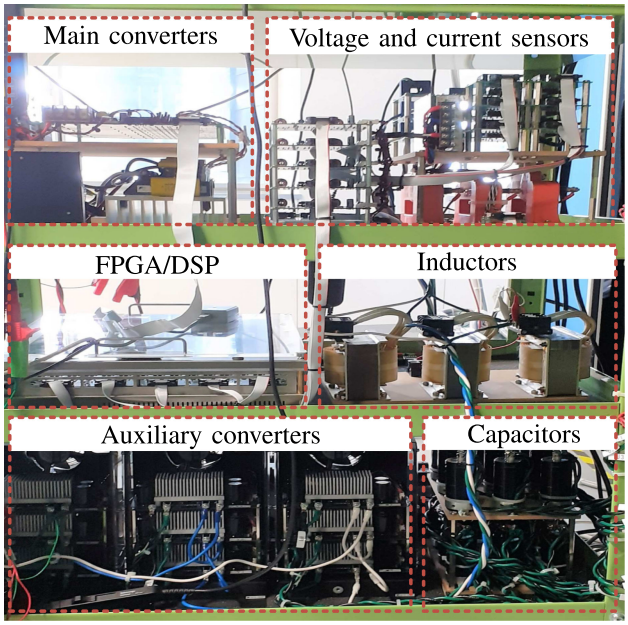

Fig. 7. Photograph of the down-scaled model used in experiments.

similar to $v_{\rm M1}$ in shape except that the phase-shift of 120° (= 360°/3) exists between them.

The carrier frequency of the IGBTs used in the main converters was set to $f_{\rm SM} = 900$ Hz, and the carrier frequency of the power MOSFETs used in the auxiliary converters was set to $f_{\rm SA} = 3.6$ kHz. The bridge-cell count in each auxiliary converter was set to $m = 3$ which makes the equivalent switching frequency of each auxiliary converter become 21.6 kHz ($= 2mf_{\rm SA}$). The capacitance of each full-bridge capacitor was set to 2.5 mF, and the voltage reference of each dc-capacitor voltage was set to $v^*_{Cij} = 50$ V. The chopper-cell count was set to $n = 3$ which makes the equivalent switching frequency of the main converters become 2.7 kHz ($= nf_{\rm SM}$). The high-voltage-side capacitor was set to $C_{\rm dc} = 4.8$ mF, where the capacitor and parasitic impedance of the voltage source work as a passive filter to mitigate the ripple current in $i_{\rm dc1}$. Each inductor presents the inductance of 0.75 mH at 0 Hz; however, it is reduced to 0.32 mH at 21.6 kHz (i.e., the equivalent switching frequency of the auxiliary converter) owing to its frequency characteristics.

The high- and low-voltage sides are connected to dc power supplies (NF DP030RS), and each dc capacitor was kept at an initial voltage of 50 V prior to the start of the experiments.

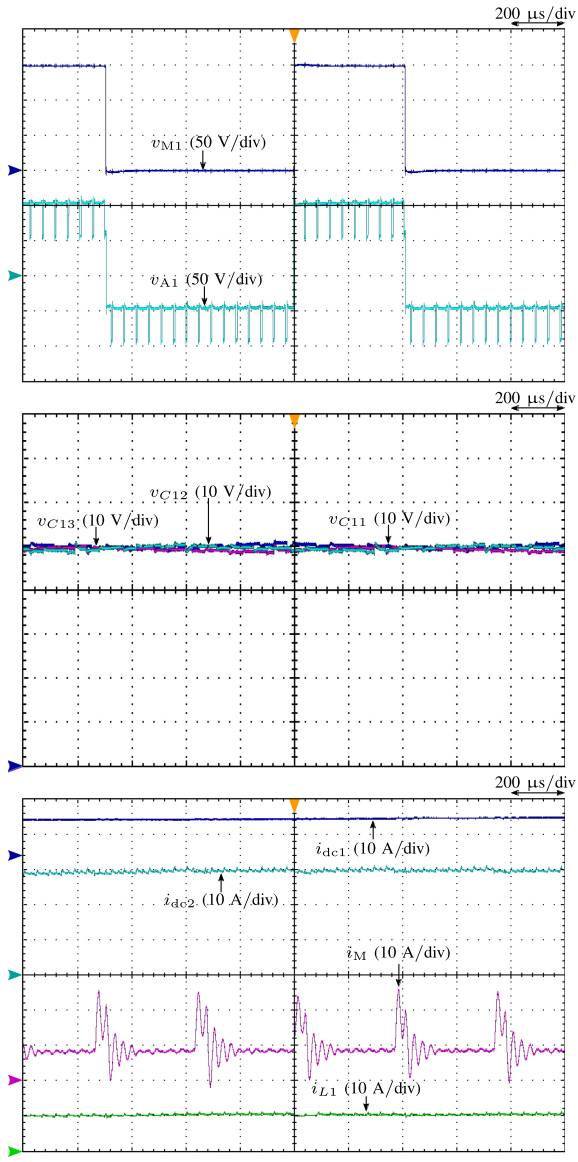

Fig. 8. Experimental waveforms of the IBCAC when $i^*_{\rm dc2} = 30$ A, and $v_{\rm dc2} = 50$ V.

For Figs. 8 to 10, the experimental waveforms of $v_{\rm M1}$ and $v_{\rm A1}$ were taken by the Tektronix oscilloscope DPO4034B with a frequency band of 350 MHz. The experimental waveforms of $i_{\rm dc1}$, $i_{\rm dc2}$, $i_{\rm M}$, and i_{L1} were taken by the Tektronix oscilloscope MDO4104C with a frequency band of 1 GHz. The experimental waveforms of v_{C11}, v_{C12}, and v_{C13} were taken by the Tektronix oscilloscope DPO3054 with a frequency band of 500 MHz. The Tektronix current probes TCP0150, TCP303, TCP0030A, and TCP0020 were used for the measurement of $i_{\rm dc1}$, $i_{\rm dc2}$, $i_{\rm M}$, and i_{L1}, respectively. The Tektronix voltage probes THDP0200 were used for the measurement of v_{C11}, v_{C12}, v_{C13}, and $v_{\rm A1}$, while the Tektronix voltage probe THDP0100 was used to measure $v_{\rm M1}$. For Figs. 11 to 13, the experimental waveforms were taken by Tektronix oscilloscope DPO4104B-L with a frequency band of 1 GHz. The Tektronix voltage probes THDP0200 were used for the measurement of $v_{\rm M1}$, $v_{\rm A1}$, v_{C11}, v_{C21}, and

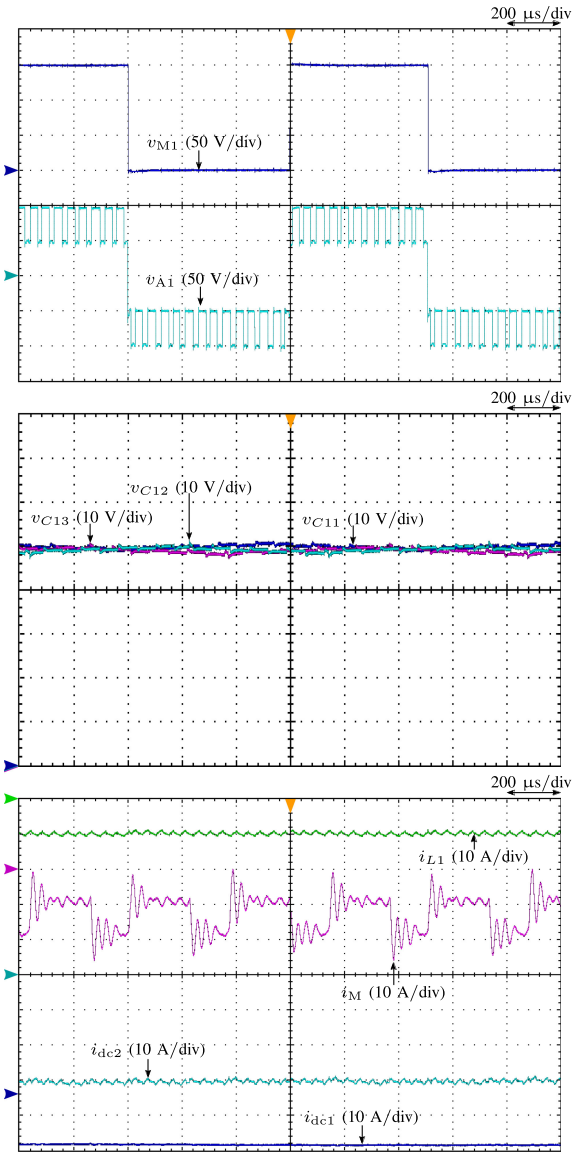

Fig. 9. Experimental waveforms of the IBCAC when $i^*_{dc2} = -30$ A, and $v_{dc2} = 75$ V.

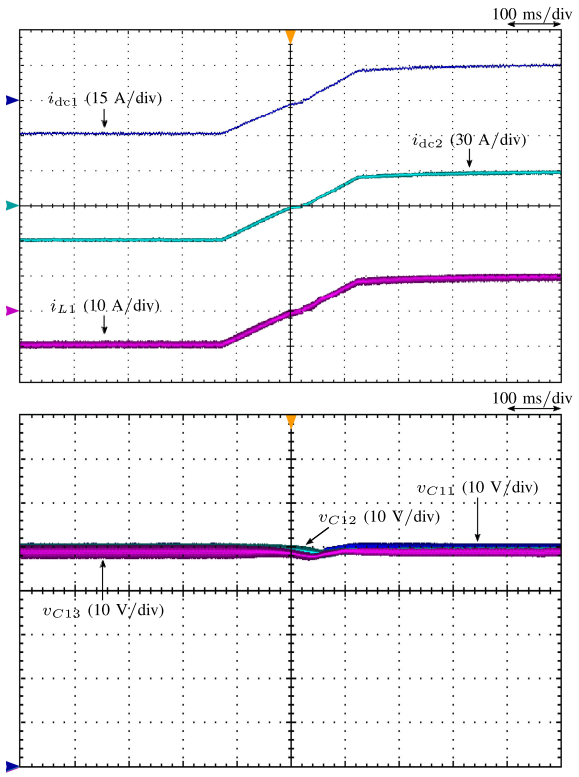

Fig. 10. Experimental waveforms of the IBCAC when $v_{dc2} = 75$ V, where i^*_{dc2} was changed from -30 to 30 A in 250 ms.

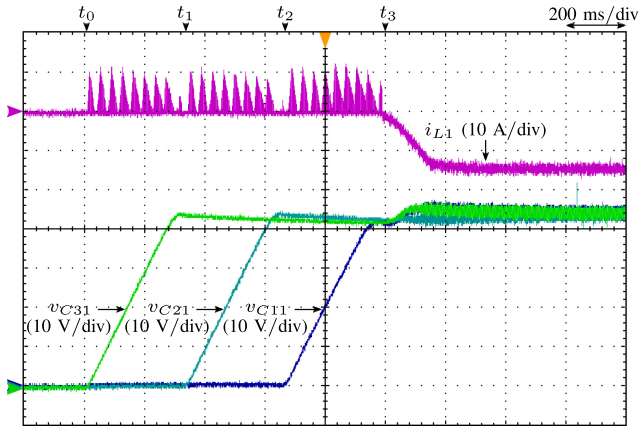

Fig. 11. Experimental waveforms during startup when $i^*_L = -15$ A.

v_{C31}. The Tektronix current probe TCP0030A was used for the measurement of i_{L1}. The control system consists of a digital signal processor (DSP) unit using the Texas Instruments TMS320C6678 and a field-programmable gate array (FPGA) unit using the Altera Cyclone IV. The FPGA unit including A/D converters detects the nine dc-capacitor voltages of the full-bridge converters, the three inductor currents, and the high- and the low-voltage-side dc voltages. The FPGA unit produces 42 gate signals in total. The sampling and reference update period of the control system was set to 46.3 μms $(= 1/(2mf_{SA}))$.

B. Steady-State Operation When $i_{dc2} > 0$

Fig. 8 shows the experimental waveforms of the IBCAC during a steady-state operation when $i^*_{dc2} = 30$ A, and $v_{dc2} = 50$ V. The active power is flowing from the high-voltage side to the low-voltage side, which models the charging operation of BESS in an actual system. The voltage produced by the main converter, v_{M1}, is a square wave containing both dc and ac components, where the frequency of the ac components is 900 Hz. The duty ratio, d_{M1}, is slightly larger than 0.33 $(= v_{dc2}/v_{dc1})$, owing to the additional voltage components stemming from the current feedback control and v^*_{B1} shown in Fig. 5.

The voltage produced by the auxiliary converter, v_{A1}, is a square wave with a dominant frequency of 900 Hz. In addition, it contains a switching-ripple component with a frequency of 21.6 kHz $(= 2mf_{SA})$ and a voltage step of 50 V $(= v_{Cij})$ stemming from the phase-shifted PWM.

The 900-Hz ac components included in v_{M1} and v_{A1} cancel out each other, and no ac voltage appears in the inductor voltage

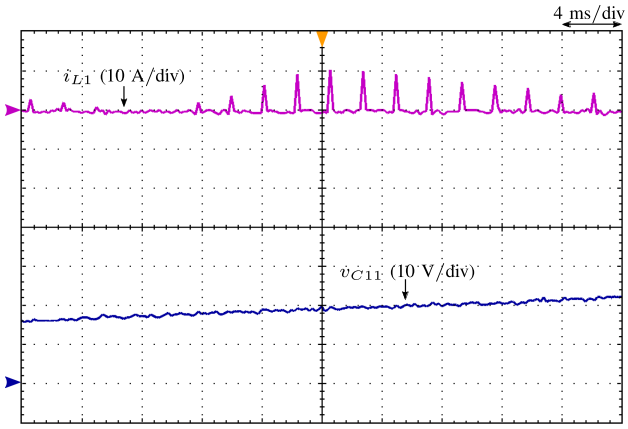

Fig. 12. Time-expanded waveforms during the initial charging of v_{C11}.

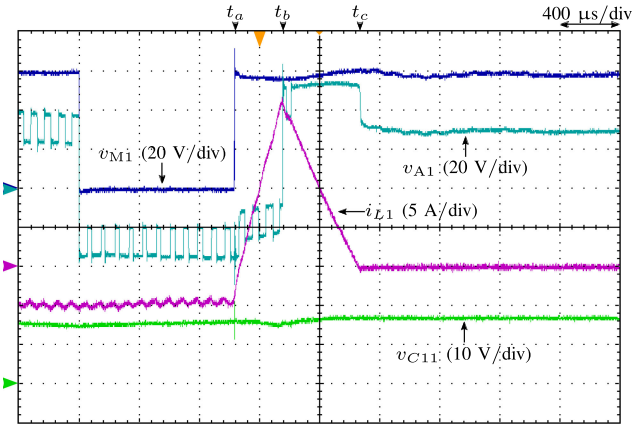

Fig. 13. Experimental waveforms during circuit breaker operation.

except for a small amount of switching-ripple voltage with a frequency of 21.6 kHz. Consequently, the switching-ripple current in the inductor current can be mitigated satisfactorily.

The dc-capacitor voltages, v_{C11}, v_{C12}, and v_{C13}, contain a dc component that is regulated to 50 V without any steady-state error by the auxiliary converters. In addition, a triangular-wave ac component with a dominant frequency of 900 Hz exists in each dc-capacitor voltage. However, this ac component is less than 1/10 in a peak-to-peak value compared with the dc component of 50 V.

The total current flowing to the main converters, $i_{\rm M}$, consists of a dc component of 10 A and an ac component with a frequency of 2.7 kHz $(= nf_{\rm SM})$. It is noteworthy that no ac component would be included in $i_{\rm M}$ when the relations $n = 3$ and $d_{\rm M1} = d_{\rm M2} = d_{\rm M3} = v_{\rm dc2}/v_{\rm dc1} = 0.33$ hold because the perfect cancellation of the ac components in $i_{\rm M1}$, $i_{\rm M2}$, and $i_{\rm M3}$ occurs in this case. However, each duty ratio is slightly larger than 0.33 as mentioned above, and an amount of ac component occurs in $i_{\rm M}$. Specifically, a surge current with a frequency of 21.6 kHz occurs in $i_{\rm M}$, and it is attenuated with the passage of time as shown in Fig. 8. Meanwhile, the dc current sourced from $v_{\rm dc1}$, $i_{\rm dc1}$, is a dc current containing no ac component owing to a good effect of the capacitor, $C_{\rm dc}$, and the parasitic inductance of the dc source working as a passive filter.

The dc current flowing to $v_{\rm dc2}$, $i_{\rm dc2}$, is controlled indirectly by controlling the individual inductor currents, i_{Lj}, such that $1/n$ of $i_{\rm dc2}$ flows through each inductor. Fig. 8 shows that i_{L1} and $i_{\rm dc2}$ are regulated at 10 and 30 A, respectively, without any steady-state error.

C. Steady-State Operation When $i_{\rm dc2} < 0$

Fig. 9 shows the experimental waveforms of the IBCAC during a steady-state operation when $i^*_{\rm dc2} = -30$ A, and $v_{\rm dc2} = 75$ V. The active power is flowing from the low-voltage side to the high-voltage side, which models the discharging operation of BESS in an actual system. The voltage and current waveforms are similar to those of Fig. 8 except for the current polarity changed. Unlike Fig. 8, the duty ratio, $d_{\rm M1}$, is slightly smaller than 0.5 $(= v_{\rm dc2}/v_{\rm dc1})$ owing to v^*_{B1} changed to a negative value. This interesting phenomenon occurs because the polarity of v^*_{B1} changes according to that of the inductor current as shown in Fig. 6.

The dc component included in the dc-capacitor voltages v_{C11}, v_{C12}, and v_{C13} are regulated to 50 V without any steady-state error. $i_{\rm dc1}$ is a pure dc current and it is obtained as -14 A, which is slightly smaller than the theoretical value of -15 A $(= -2.25\,{\rm kW}/150\,{\rm V})$ owing to the converter loss. $i_{\rm M}$ is a square wave with a dominant frequency of 2.7 kHz, and it also contains a surge current with a frequency of 21.6 kHz similar to Fig. 8.

D. Transient Performance During a Ramp Change in $i_{\rm dc2}$

Fig. 10 shows the experimental waveforms of the IBCAC during a transient-state operation when $v_{\rm dc2} = 75$ V, where $i^*_{\rm dc2}$ was changed from -30 to 30 A in 250 ms under a ramp change. Fig. 10 shows that $i_{\rm dc1}$, i_{L1}, and $i_{\rm dc2}$ changed without any overcurrent. Carefully looking into Fig. 10 reveals that the gradient of each current decreases when they approach zero. This interesting phenomenon occurs owing to the effect of ON-state voltages of power devices used in the auxiliary converters. This effect can be mitigated by applying the conventional ON-state voltage drop compensation method, where the polarity of the compensation voltage is changed according to the polarity of the inductor current.

The dc components included in each dc-capacitor voltage were regulated to 50 V without any error even during the transient state. Meanwhile, the amplitude of the ac components included in each dc-capacitor voltage decreased as the inductor current approached zero, and increased again as the inductor current approached its reference current of 10 A. This phenomenon occurs because the amplitude of the ac components is proportional to that of the inductor current.

E. Converter Operation During Startup

The waveforms of one subconverter are shown in the following section because the converter operation during startup is identical among the three subconverters. In addition, the carrier frequencies were changed to $f_{\rm SM} = 450$ Hz and $f_{\rm SA} = 1.8$ kHz and the inductance value of L_1 was changed from 0.75 to 0.5 mH

TABLE III
SEQUENCE OF INITIAL CHARGING

Period	$t_0 \le t < t_1$	$t_1 \le t < t_2$	$t_2 \le t < t_3$
Process	v_{C31} charging	v_{C21} charging	v_{C11} charging
Cell 11 Mode	short-circuit	short-circuit	charging
Cell 21 Mode	short-circuit	charging	short-circuit
Cell 31 Mode	charging	short-circuit	short-circuit

for convenience; however, this change does not affect to the converter operation.

Fig. 11 shows the experimental waveforms of v_{C11}, v_{C21}, v_{C31}, and i_{L1} during the converter startup. In this experiment, the initial charging of the capacitors was realized using $v_{\rm dc1}$ and the relation $i_{L1} \ge 0$ holds through the charging process. In this case, $\mathrm{S_{u}}_j$ is the active switch that controls the charging process and $\mathrm{S_{l}}_j$ is kept OFF. Before t_0, all capacitor voltages are set to zero. The charging process starts at t_0 according to a sequence depicted in Table III, where the time instants t_1, t_2, and t_3 represent the end-of-charging instants of v_{C31}, v_{C21}, and v_{C11}, respectively.

During t_0 to t_1, the voltage reference for v_{C31} increased from zero to 45 V under a ramp change in approximately 0.4 s. Fig. 12 shows the time-expanded waveforms of Fig. 11 during the initial charging of v_{C11}. In this period, the cell 21 and cell 31 are operating in the short-circuit mode and the cell 11 is operating in the charging mode shown in Table I. Meanwhile, the duty ratio of the main converter, $d_{\rm M1}$, is determined by the feedback control of v_{C11} and its reference voltage, v^*_{C11}. $d_{\rm M1}$ is proportional to $v^*_{C11} - v_{C11}$, and the inductor current increases linearly with a gradient of $(v_{\rm dc1} - v_{\rm dc2})/L_1$ when $\mathrm{S_{u1}}$ is on. Consequently, v_{C11} increases. When $\mathrm{S_{u1}}$ is OFF, the inductor current decreases linearly with a gradient of $-v_{\rm dc2}/L_1$ via a freewheeling diode in $\mathrm{S_{l1}}$, and it becomes zero finally. However, v_{C11} keeps increasing during this period since the relation $i_{L1} \ge 0$ holds. After the inductor current becomes zero, v_{C11} is kept to a constant value until $\mathrm{S_{u1}}$ turns ON again. This charging process is repeated every switching period of the main converter $(= 1/f_{\rm SM} = 2.2\,\mathrm{ms})$ until v_{C11} reaches 45 V. When the initial charging finishes, power transfer can be initiated. In this experiment, a ramp signal that decreases from 0 to -15 A in 0.2 s was selected as a current reference. It can be concluded from Fig. 11 that the converter startup including the initial charging can be achieved successfully without any overvoltage or overcurrent.

F. Circuit Breaker Operation

The waveforms of one subconverter are shown in the following section because the circuit breaker operation is identical among the three subconverters. In addition, the carrier frequencies were changed to $f_{\rm SM} = 450$ Hz and $f_{\rm SA} = 1.8$ kHz, and the inductance value of L_1 was changed from 0.75 to 0.5 mH. In the following, a short-circuit fault is assumed to occur in $\mathrm{S_{u1}}$, and this fault can be imitated by turning $\mathrm{S_{u1}}$ ON at a certain time point. Simultaneously, $\mathrm{S_{l1}}$ is turned OFF for preventing a short-circuit current from flowing at the high-voltage side. The relations $v_{\rm dc1} = 60$ V, $v_{\rm dc2} = 30$ V, $v_{Ci1} = 15$ V, and $i_{L1} = -5$ A hold prior to the fault occurrence. Fig. 13 shows the experimental waveforms during the circuit breaker operation where the fault occurred at t_a. $\mathrm{S_{u1}}$ and $\mathrm{S_{l1}}$ are kept ON and OFF, respectively, after t_a. The following circuit equation holds in Fig. 2(a) after t_a

$$\frac{di_{L1}}{dt} = \frac{1}{L_1}(v_{\rm dc1} - v_{\rm dc2} - v_{\rm A1}). \tag{13}$$

In (13), $v_{\rm A1}$ is the sum of voltage components produced by the dc-capacitor voltage control and ripple current mitigation, where the former is given by (11) and the latter is given by (4), respectively. The relation $(v_{\rm A1})_{\rm ac} \gg v_{B1}(= v^*_{B1})$ holds just after t_a because the relation $v^*_{Cij} = (v_{Cij})_{\rm dc}$ holds before t_a. Hence, the reasonable approximation of $v_{\rm A1} \approx (v_{\rm A1})_{\rm ac}$ can be applied. Equation (4) means that $(v_{\rm A1})_{\rm ac}$ can be $(1 - d_{\rm M1})v_{\rm dc1}$ or $-d_{\rm M1}v_{\rm dc1}$ according to the operating conditions. Fig. 13 shows that the relation $(v_{\rm A1})_{\rm ac} = -d_{\rm M1}v_{\rm dc1}$ holds just after t_a. Substituting the relations $d_{\rm M1} \approx v_{\rm dc2}/v_{\rm dc1} = 0.5$ and $v_{\rm dc1} = 60$ V into $(v_{\rm A1})_{\rm ac} = -d_{\rm M1}v_{\rm dc1}$ produces $v_{\rm A1} = (v_{\rm A1})_{\rm ac} = -30$ V. Substituting the relations $v_{\rm dc1} = 60$ V, $v_{\rm dc2} = 30$ V, $v_{\rm A1} = -30$ V, and $L_1 = 0.5$ mH into (13) yields $di_{L1}/dt = 120$ A/s. It is higher than $di_{L1}/dt = 84.4$ A/s obtained from Fig. 13 because $v_{\rm A1}$ increases from -30 V after t_a as shown in Fig. 13 owing to the effect of the voltage component given by (11). When i_{L1} reaches a threshold value of 22 A, all power devices in the auxiliary converter are turned OFF at t_b. Subsequently, i_{L1} starts to flow into the cell capacitors via the free-wheeling diodes in $\mathrm{S_{u1}}$ and $\mathrm{S_{l1}}$. Therefore, the following equation holds in Fig. 2(a):

$$\frac{di_{L1}}{dt} = \frac{1}{L_1}\left(v_{\rm dc1} - v_{\rm dc2} - \sum_{i=1}^{3} v_{Ci1}\right). \tag{14}$$

Substituting the relations $v_{\rm dc1} = 60$ V, $v_{\rm dc2} = 30$ V, $v_{C11} + v_{C21} + v_{C31} = 51$ V, and $L_1 = 0.5$ mH into (13) yields $di_{L1}/dt = -42$ A/s, which agrees well with $di_{L1}/dt = -42.3$ A/s obtained from Fig. 13. i_{L1} reached zero at t_c, and all the electromagnetic energy stored in the circuit was stored or dissipated at the capacitors or parasitic resistance. After t_c, the relation $v_{\rm A1} = v_{\rm dc1} - v_{\rm dc2}$ holds, and the circuit breaker operation is completed. The time interval from the fault inception to fault clearance is 0.84 ms, which is faster than that of the conventional mechanical circuit breaker shown in Fig. 2(a).

G. Measured Efficiency of the Downscaled Experimental Model

Fig. 14 (a) shows the measured efficiency of the experimental downscaled model of the IBCAC with different output power references. It can be shown that the efficiency of the downscaled model can reach as high as approximately 95%. Fig. 14 (b) shows the measured efficiency with different voltage gains, where $v_{\rm dc1}$ equals 150 V and $i_{\rm dc2}$ equals 30 A. It is worth mentioning that the design of the downscaled model is not optimized. Therefore, its efficiency is expected to be lower than that of an actual system. However, the efficiency measurements are presented to give a sense of the expected efficiency of the system.

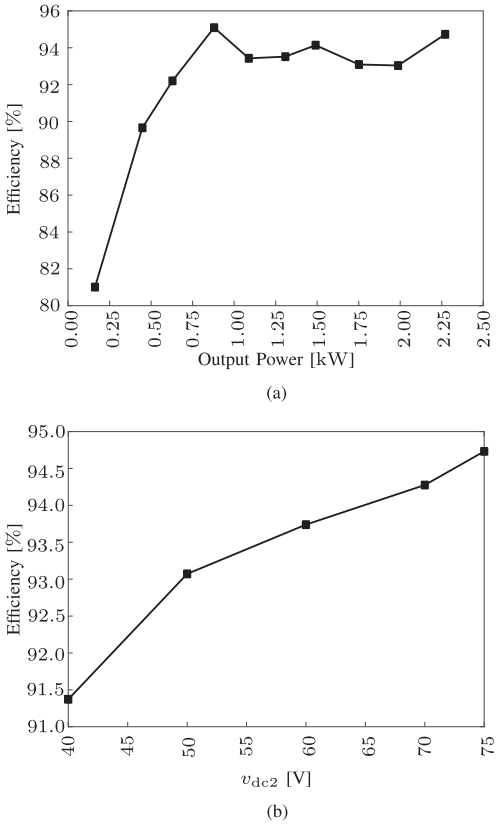

Fig. 14. Measured efficiency of the IBCAC. (a) With different output power references. (b) With different voltage gains.

VI. Comparison With the Conventional Interleaved Chopper

This section compares the IBCAC and the conventional interleaved bidirectional chopper, which is hereinafter referred to as the conventional chopper, in terms of mass, volume, and efficiency. The cost comparison is beyond the scope of this article and left for the future work. For achieving a fair comparison, the following conditions are assumed.

1) P, $v_{\rm dc1}$, $v_{\rm dc2}$, n, and $f_{\rm SM}$ are common to both converters.
2) L_j is selected such that the same peak-to-peak current occurs in $i_{\rm dc2}$.
3) Mass and volume of the cooling system and inductors are considered for estimation of mass and volume of the conventional chopper. Meanwhile, mass and volume of the capacitors of the full-bridge cells, inductors, cooling systems of the main and auxiliary converters are considered for estimation of mass and volume of the IBCAC.

Further, the following conditions are assumed.

1) Air-core inductors are assumed to be used in both converters because they are typically used in the railway converters [26], and both inductors are designed based on [27].
2) The cooling system is designed based on a parameter called the cooling system performance index (CSPI) [28], and this value was set to seven which is a little lower than the value used in [29].

TABLE IV
Circuit Parameters of an Actual System Used for Comparison

Rated power	P	225 kW
DC voltage source 1	$v_{\rm dc1}$	1.5 kV
DC voltage source 2	$v_{\rm dc2}$	0.75 kV
Inductance (conventional chopper)	L_j	9.4 mH
Inductance (IBCAC)	L_j	0.75 mH
Bridge-cell count in each aux. conv.	m	3
Chopper-cell count	n	3
DC-capacitor voltage	v_{Cij}	0.5 kV
Full-bridge cell capacitor	C_{ij}	2.5 mF
Carrier freq. (chopper cells)	$f_{\rm SM}$	900 Hz
Carrier freq. (auxiliary conv.)	$f_{\rm SA}$	3.6 kHz

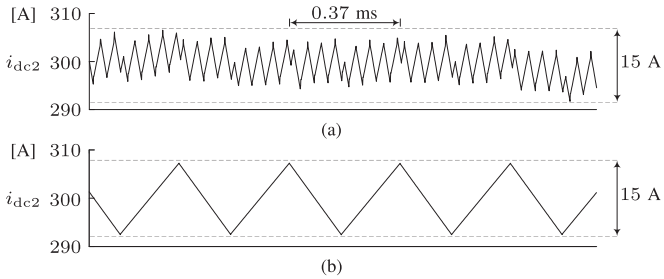

Fig. 15. Comparison of $i_{\rm dc2}$. (a) For the IBCAC with $L_j = 0.75$ mH. (b) For the conventional chopper with $L_j = 9.4$ mH.

3) The switching and conduction losses of the main converters and inductor copper loss are considered for calculating the efficiency of the conventional chopper. Meanwhile, the switching and conduction losses of the main and auxiliary converters, and inductor copper loss are considered for calculating the efficiency of the IBCAC.

Table IV summarizes the circuit parameters of an actual converter system used for comparison, where the relations $P = 225\,\text{kW}, v_{\rm dc1} = 1.5\,\text{kV}, v_{\rm dc2} = 0.75\,\text{kV}, n = 3$, and $f_{\rm SM} = 900$ Hz hold. Further, the bridge-cell count and the carrier frequency of each bridge cell are set to $m = 3$ and $f_{\rm SA} = 3.6$ kHz, respectively. Hence, the number of power devices used in each subconverter is two in the conventional chopper and 14 (2: High voltage, 12: Low voltage) in the IBCAC. Fig. 15 shows the comparison of $i_{\rm dc2}$, where Fig. 15(a) shows the waveform of the IBCAC and Fig. 15(b) shows that of the conventional chopper. Both waveforms contain a dc current of 300 A, and a triangular ac current with a peak-to-peak value of approximately 15 A. It is noteworthy that the ripple frequency of $i_{\rm dc2}$ is different in both converters; it is 2.7 kHz $(= nf_{\rm SM})$ in the conventional chopper and 21.6 kHz $(= 2mf_{\rm SA})$ in the IBCAC. This implies that the mass and volume of a filter for removing this ripple current from $i_{\rm dc2}$ can be reduced by applying the IBCAC. The inductance value is set to $L_j = 9.4$ mH in the conventional chopper, and set to $L_j = 0.75$ mH in the IBCAC, where the Brooks inductors are assumed to be used. Hence, the inductance value can be reduced by 12.5 times using the auxiliary converters.

The power devices MBM250H33E3T (Si-IGBT, 2-in-1, 3.3 kV) manufactured by Hitachi are assumed to be used in the main converter, where the device characteristics are provided in [30]. The power devices 2MBI200XAA120-50 (Si-IGBT,

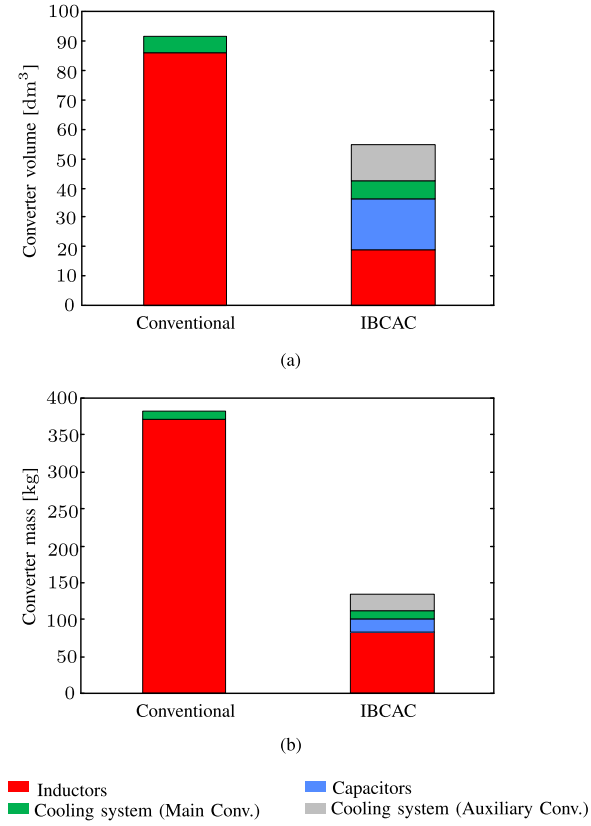

Fig. 16. Comparison between the conventional chopper and the IBCAC in terms of (a) volume and (b) mass.

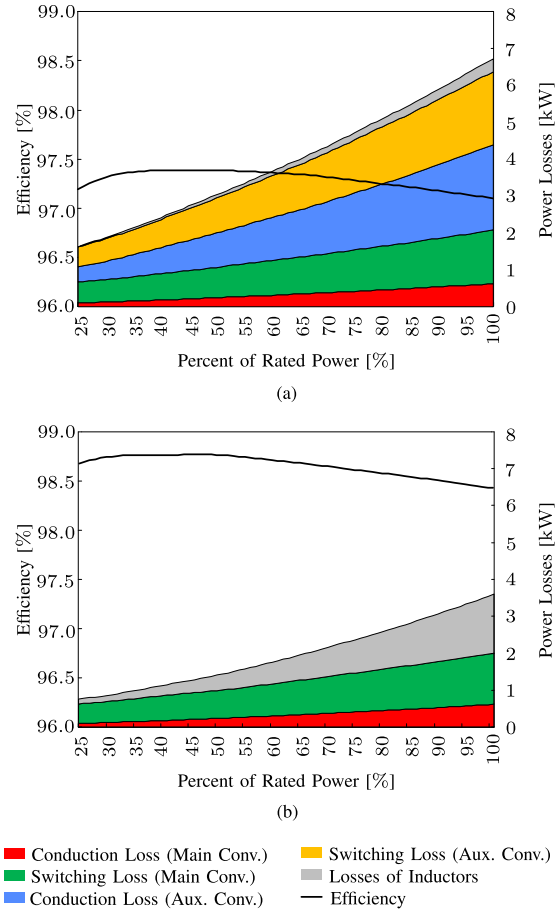

Fig. 17. Efficiency and loss breakdown. (a) IBCAC. (b) The conventional chopper.

2-in-1, 1.2 KV) manufactured by Fuji Electric are assumed to be used in the auxiliary converter, where the device characteristics are provided in [31]. The following conditions are considered.

1) Conduction loss, turn-ON/OFF switching loss are considered in IGBTs, and the conduction loss and turn-OFF switching loss are considered in diodes.
2) Conduction loss and switching loss are calculated based on voltage, current, loss characteristics that were obtained from the datasheets of the power devices, where the maximum junction temperature was set to 125° C and the ambient temperature was set to 40° C.

A 600 V, 2.53 mF dc film capacitor (E50.R18-255NT0) manufactured by Electronicon is assumed to be used in each full-bridge cell, where its specifications are provided in [32]. After the converter systems were designed, total power losses of each converter system were estimated. Further, the mass and volume of the inductors and the auxiliary converters were estimated. It should be mentioned that the mass of cooling system was estimated by assuming that the density of heatsinks is 2/3 the density of aluminum.

Fig. 16(a) shows a comparison between the total volume of components of the conventional chopper and the IBCAC. Similarly, Fig. 16(b) shows the same comparison in terms of mass. In Fig. 16, the volume is reduced by 40.3% and the mass is reduced by 64.8%. When the replacement of the low-voltage-side dc-circuit breaker by the auxiliary converters is taken into consideration, the reduction of volume and mass of the whole converter system becomes more significant.

The efficiency of the proposed chopper is expected to be lower than that of the conventional chopper since more power devices are employed. Fig. 17 shows the efficiency curves of both the proposed and conventional choppers where it can be shown that the reduction in efficiency is not that significant. Meanwhile, the reduction of the mass of the chopper that is placed in a moving train car can lead to a reduction in the power that is required to move the train, which may lead to an improvement in the overall system efficiency.

VII. Conclusion

This article has presented an interleaved bidirectional chopper topology for high-power applications. The proposed chopper employs cascaded full-bridge cells as auxiliary converters to cancel out the undesired ac components produced by the bidirectional chopper cells. It has been shown that the proposed chopper is significantly smaller in volume and mass than the conventional interleaved bidirectional chopper. The validity of the proposed chopper has been confirmed by experiments using an experimental downscaled model.

REFERENCES

[1] M. Forouzesh, Y. P. Siwakoti, S. A. Gorji, F. Blaabjerg, and B. Lehman, "Step-up DC-DC Converters: A comprehensive review of voltage-boosting techniques, topologies, and applications," *IEEE Trans. Power Electron.*, vol. 32, no. 12, pp. 9143–9178, Dec. 2017.

[2] W. Qian, H. Cha, F. Z. Peng, and L. M. Tolbert, "55-kW variable 3X DC–DC converter for plug-in hybrid electric vehicles," *IEEE Trans. Power Electron.*, vol. 27, no. 4, pp. 1668–1678, Apr. 2012.

[3] Z. Li, S. Hoshina, N. Satake, and M. Nogi, "Development of DC/DC converter for battery energy storage supporting railway DC feeder systems," *IEEE Trans. Ind. Appl.*, vol. 52, no. 5, pp. 4218–4224, Sep./Oct. 2016.

[4] G. Cui *et al.*, "Supercapacitor integrated railway static power conditioner for regenerative braking energy recycling and power quality improvement of high-speed railway system," *IEEE Trans. Transp. Electrific.*, vol. 5, no. 3, pp. 702–714, Sep. 2019.

[5] S. de la Torre, A. J. Sánchez-Racero, J. A. Aguado, M. Reyes, and O. Martínez, "Optimal sizing of energy storage for regenerative braking in electric railway systems," *IEEE Trans. Power Syst.*, vol. 30, no. 3, pp. 1492–1500, May 2015.

[6] J. A. Aguado, A. J. S. Racero, and S. de la Torre, "Optimal operation of electric railways with renewable energy and electric storage systems," *IEEE Trans. Smart Grid*, vol. 9, no. 2, pp. 993–1001, Mar. 2018.

[7] T. Suzuki, H. Hayashiya, T. Yamanoi, and K. Kawahara, "Application examples of energy saving measures in Japanese DC feeding system," in *Proc. Int. Power Electron. Conf.*, Hiroshima, Japan, 2014, pp. 1062–1067.

[8] H. Alnuman, D. T. Gladwin, and M. P. Foster, "Novel control method for improving energy efficiency of DC electric railways," in *Proc. Int. Conf. Control Autom.*, Edinburgh, U.K., 2019, pp. 91–96.

[9] T. Konishi and M. Tobita, "Fixed energy storage technology applied for DC electrified railway (traction power substation)," in *Proc. Elect. Syst. Aircraft, Railway Ship Propulsion*, Bologna, Italy, 2012, pp. 1–6, doi: 10.1109/ESARS.2012.6387438.

[10] H. Hayashiya *et al.*, "Possibility of energy saving by introducing energy conversion and energy storage technologies in traction power supply system," in *Proc. 15th Eur. Conf. Power Electron. Appl.*, Lille, France, 2013, pp. 1–8, doi: 10.1109/EPE.2013.6631780.

[11] D. Iannuzzi and P. Tricoli, "Speed-based state-of-charge tracking control for metro trains with onboard supercapacitors," *IEEE Trans. Power Electron.*, vol. 27, no. 4, pp. 2129–2410, Apr. 2012.

[12] F. Ciccarelli, A. D. Pizzo, and D. Iannuzzi, "Improvement of energy efficiency in light railway vehicles based on power management control of wayside lithium-ion capacitor storage," *IEEE Trans. Power Electron.*, vol. 29, no. 1, pp. 275–286, Jan. 2014.

[13] H. Hayashiya *et al.*, "Proposal of a novel control method of Li-ion battery system for regenerative energy utilization in traction power supply system," in *Proc. Int. Power Electron. Motion Control Conf.*, Varna, Bulgaria, 2016, pp. 298–303.

[14] K. Ogura, K. Nishimura, and Y. Oku, "A bidirectional DC–DC converter for battery electric light rail vehicle and its test run results," in *Proc. IEEE Int. Conf. Power Electron. Drive Syst.*, Toulouse, France, 2019, pp. 1–6, doi: 10.1109/PEDS44367.2019.8998957.

[15] D. Ronanki, S. A. Singh, and S. S. Williamson, "Comprehensive topological overview of rolling stock architectures and recent trends in electric railway traction systems," *IEEE Trans. Transp. Electrific.*, vol. 3, no. 3, pp. 724–738, Sep. 2017.

[16] A. Gmez-Expsito, J. M. Mauricio, and J. M. Maza-Ortega, "VSC-based MVDC railway electrification system," *IEEE Trans. Power Del.*, vol. 29, no. 1, pp. 422–431, Feb. 2014.

[17] A. Verdicchio, P. Ladoux, H. Caron, and C. Courtois, "New medium-voltage DC railway electrification system," *IEEE Trans. Transp. Electrific.*, vol. 4, no. 2, pp. 591–604, Jun. 2018.

[18] L. Ni, D. J. Patterson and J. L. Hudgins, "High power current sensorless bidirectional 16-phase interleaved DC–DC converter for hybrid vehicle application," *IEEE Trans. Power Electron.*, vol. 27, no. 3, pp. 1141–1151, Mar. 2012.

[19] P.-L. Wong, P. Xu, P. Yang, and F. C. Lee, "Performance improvements of interleaving VRMs with coupling inductors," *IEEE Trans. Power Electron.*, vol. 16, no. 4, pp. 449–507, Jul. 2001.

[20] P.-L. Wong, F. C. Lee, P. Xu, and K. Yao, "Critical inductance in voltage regulator modules," *IEEE Trans. Power Electron.*, vol. 17, no. 4, pp. 485–492, Jul. 2002.

[21] M. Pavlovsk, G. Guidi, and A. Kawamura, "Assessment of coupled and independent phase designs of interleaved multiphase buck/boost DCDC converter for EV power train," *IEEE Trans. Power Electron.*, vol. 29, no. 6, pp. 2693–2704, Jun. 2014.

[22] O. Hegazy, J. V. Mierlo, and P. Lataire, "Analysis, modeling, and implementation of a multidevice interleaved DC/DC converter for fuel cell hybrid electric vehicles," *IEEE Trans. Power Electron.*, vol. 27, no. 11, pp. 4445–4445, Nov. 2012.

[23] Y. Li, Y. Wang, and B. Q. Li, "Generalized theory of phase-shifted carrier PWM for cascaded h-bridge converters and modular multilevel converters," *IEEE J. Emerg. Sel. Topics Power Electron.*, vol. 4, no. 2, pp. 598–605, Jun. 2016.

[24] S. K. Sahoo and T. Bhattacharya, "Phase-shifted carrier-based synchronized sinusoidal PWM techniques for a cascaded H-bridge multilevel inverter," *IEEE Trans. Power Electron.*, vol. 33, no. 1, pp. 513–524, Jan. 2018.

[25] Y. Liang and C. O. Nwankpa, "A new type of STATCOM based on cascading voltage-source inverters with phase-shifted unipolar SPWM," *IEEE Trans. Ind. Appl.*, vol. 35, no. 5, pp. 1118–1123, Sep.\Oct. 1999.

[26] G. Abad, *Power Electronics and Electric Drives for Traction Applications*. Hoboken, NJ, USA: Wiley, 2016.

[27] R. Barrera-Cardenas, T. Isobe, and M. Molinas, "Optimal design of air-core inductor for medium/high power DC-DC converters," in *Proc. IEEE 17th Workshop Control Model. Power Electron.*, Trondheim, Norway, 2016, pp. 1–8, doi: 10.1109/COMPEL.2016.7556774.

[28] U. Drofenik and J. W. Kolar, "Thermal power density barriers of converter systems," in *Proc. 5th Int. Conf. Integr. Power Electron. Syst.*, Nuremberg, Germany, 2008, pp. 1–5.

[29] A. Hillers, M. Stojadinovic, and J. Biela, "Systematic comparison of modular multilevel converter topologies for battery energy storage systems based on split batteries," in *Proc. 17th IEEE Euro. Conf. Power Electron. Appl.*, Geneva, Switzerland, 2015, pp. 1–9, doi: 10.1109/EPE.2015.7309385.

[30] Hitachi. Tokyo, Japan, *IGBT Module*. 2020. [Online]. Available: https://www.hitachi-power-semiconductor-device.co.jp/en/products/igbt/pdf/IGBT-SP-12023R6_MBM250H33E3_web.pdf

[31] Fuji Electric, Tokyo, Japan, *IGBT Module*. 2020. [Online]. Available: https://americas.fujielectric.com/wp-content/uploads/2020/06/2MBI200XAA120-50.pdf

[32] Electronicon, Kondensatoren GmbH, Germany. *PK16, GA85, E61 High Density DC Film Capacitors.* 2020. [Online]. Available: https://www.electronicon.com/fileadmin/inhalte/pdfs/downloadbereich/Katalog/neue_Kataloge_2011/200.003-020030_PK16.pdf

Hamzeh J. Ahmad (Student Member, IEEE) was born in Amman, Jordan, in 1991. He received the B.S. degree in electrical engineering from Hashemite University, Jordan, in 2013, and M.S. degree in electrical engineering\power and control from Jordan University of Science and Technology Irbid, Jordan, in 2016. He has been working toward the Ph.D. degree in electrical and electronic engineering with Tokyo Institute of Technology, Japan, since April 2018.

His research interests include high-power dc-to-dc converters for electric trains/vehicles, dc-to-ac converters for utility applications, solid-state circuit breakers, and control of power converters.

Makoto Hagiwara (Senior Member, IEEE) was born in Tokyo, Japan, in 1979. He received the B.S., M.S., and Ph.D. degrees in electrical engineering from Tokyo Institute of Technology Tokyo, Japan, in 2001, 2003, and 2006 respectively.

From April 2006 to March 2015, he was an Assistant Professor with the Department of Electrical and Electronic Engineering, Tokyo Institute of Technology, and an Associate Professor, since April 2015. The total citation index for all his papers in Google Scholar is more than 5200. His research interests include dc-to-dc converters for electric trains/vehicles, high-voltage high-power converters for utility applications and renewable energies, and HVdc technologies.

Dr. Hagiwara was the recipient of the 2010 international power electronics conference (IPEC-Sapporo/ECCE-Asia) Second Prize Paper award, the 2012 and 2013 IEEE Industry Applications Society Industrial Power Converter Committee First Prize Paper Awards, and the 2014 Isao Takahashi Power Electronics Award.